INTERNATIONAL JOURNAL FOR NUMERICAL METHODS IN FLUIDS, VOL. 13, 1179–1204 (1991)

A NUMERICAL STUDY OF THE TURBULENT FLOW AROUND THE STERN OF SHIP MODELS

G. D. TZABIRAS

Department of Naval Architecture and Marine Engineering, National Technical University of Athens, 42 October 28th Street, 10682 Athens, Greece

SUMMARY

The present work is concerned with the numerical calculation of the turbulent flow field around the stern of ship models. The finite volume approximation is employed to solve the Reynolds equations in the physical domain using a body-fitted, locally orthogonal curvilinear co-ordinate system. The Reynolds stresses are modelled according to the standard k–ε turbulence model. Various numerical schemes (i.e. hybrid, skew upwind and central differencing) are examined and grid dependence tests have been performed to compare calculated with experimental results. Moreover, a direct solution of the momentum equations within the near-wall region is tried to avoid the disadvantages of the wall function approach. Comparisons between calculations and measurements are made for two ship models, i.e. the SSPA and HSVA model.

KEY WORDS Reynolds equations Finite volume methods Stern flows Turbulence modelling

INTRODUCTION

The energy-saving demands in marine transport have increased the interest in designing ship forms with favourable resistance characteristics as well as in predicting more accurately the horsepower required to obtain the specified speed for a defined ship hull. So far, the calculation of the total resistance and the related propeller–engine selection for a known ship form have been based on semi-empirical methods which extrapolate model-scale experimental data (see e.g. Reference 1). The crucial assumptions made in these methods are essentially variants of the well known Froude hypothesis[2] dividing the non-dimensional total resistance coefficient in two parts. The first part is the so-called wave-making resistance coefficient C_w, which is the same for both model and full scale since the experiments are done at a Froude number equal to that of the real ship. The remaining part is the residual resistance coefficient C_r, which includes the viscous effects (shear and pressure forces). Since the full-scale Reynolds number is about 100–1000 times higher than the model-scale value, there is a need to extrapolate the value of C_r using assumptions which, more or less, oversimplify the problem. The disadvantage of such methods becomes serious when the total resistance is mainly due to viscous effects, which is the case for many types of merchant ships. On the other hand, the development of advanced computer codes dealing with the calculation of the flow around ships has produced encouraging results in many applications. As available computing power increases, their effectiveness becomes more and more promising and they have started to be considered as the alternative for making reliable full-scale resistance predictions.

The numerical solution of the Navier–Stokes equations governing the flow field around a ship moving at steady forward speed is one of the most complicated problems of computational fluid

0271–2091/91/191179–26$13.00

Received November 1990
Revised February 1991

dynamics. The presence of the free surface, the locally unsteady propeller operation and the development of a thick boundary layer at the stern region introduce special difficulties and, till now, a solution method concerned with the complete problem has not appeared. So far, investigations have been focused on the independent treatment of each of the above aspects. Remarkable progress has been made towards the solution of the non-linear free surface problem (see e.g. Reference 3) and the calculation of the flow around a propeller (see e.g. Reference 4) in open water, using in both cases potential flow boundary element methods. Also, there are many methods, most of them recently developed,[5,6] which solve the time-averaged Reynolds equations around a ship's stern neglecting the propeller action and the free surface effect. In the latter case it is assumed that the flow has a symmetry plane which coincides with the original water plane of the ship in the still condition (double hull). The above viscous flow methods are based mainly on finite difference–finite volume approximations and differ according to the co-ordinate system used, the solution method and the turbulence model.

The most important uncertainty introduced when the Reynolds equations are solved is the application of a turbulence model. All the developed methods for stern flow calculations have used, up to now, simple mixing length and one- or two-equation isotropic eddy viscosity models, though their effectiveness is questionable. This is mainly due to numerical difficulties which had firstly to be faced, such as the velocity–pressure convergence procedure and the grid generation around the stern. Associated with the turbulence model is also the near-wall treatment. There are two methods which have been employed to calculate the flow variables near the solid boundary, i.e. the wall function method[7] or the direct solution of the transport equations up to it.[8–10] The latter is certainly more accurate but is difficult to apply in the case of a high-Reynolds-number flow past a ship owing to the prohibitive numbers of required grid nodes. In contrast, the wall function method can be adopted without particular problems to calculate these flows and seems to be valid within a wide range of near-wall grid resolutions.[11]

When comparisons are made between calculated and experimental results, it is essential to define to what extent existing differences are due either to the numerical or the turbulence modelling. There are, in general, two ways of testing the accuracy of a numerical method, i.e. the application of successively refined grids (grid dependence tests) or the employment of higher-order schemes to model terms of the discretized equations.[12] Since the effectiveness of both approaches depends mostly on the problem considered, one of the main objectives of the present work is to examine their influence on a numerical method used to solve the Reynolds equations around double-ship models. In addition, a direct solution of the momentum equations up to the solid boundary is undertaken in order to investigate if the results obtained by the wall functions can be improved. The described method, whose original versions have been reported in References 13–15, is based on the finite volume approximation. A body-fitted co-ordinate system is used to solve the transport equations in the physical domain and the Reynolds stresses are modelled according to the standard k–ε turbulence model.[16] Calculations are compared to measurements of velocity profiles, pressure and skin friction coefficients for different stern forms, i.e. the SSPA[17,18] and HSVA[19] models. A thorough experimental investigation has been carried out for both of them and well documented data are available in the open literature.

NUMERICAL METHOD

Co-ordinate system

The transport equations describing the turbulent flow around the ship are solved numerically in a calculation domain which is covered by a numerical grid which is orthogonal curvilinear on

transverse sections.[13] The grid nodes on a section are intersections of x_2- and x_3-co-ordinate lines as shown in Figure 1. In the third direction x_1 the grid is non-orthogonal, since the geometry of the sections varies along the ship. Non-orthogonal grid lines on the water plane are shown in Figure 2. The flow variables refer to locally orthogonal curvilinear co-ordinate systems which coincide with the corresponding grids on transverse sections, while their third co-ordinate line is always parallel to the ship axis of symmetry. A sequence of local co-ordinate systems is therefore created corresponding to different transverse sections of the domain. The velocity components u_2 and u_3 are parallel to the lines x_2 and x_3 respectively (Figure 1) and u_1 is always normal to the section plane.

The 2D orthogonal grid on a transverse section is generated by the conformal mapping method, transforming the section contour to a unit circle according to the method of von Kerczek and Tuck.[20] The mapping function is

$$z = \sum_{n=1}^{N} a_n \zeta^{3-2n}, \tag{1}$$

where z refers to the complex plane of the ship section and ζ refers to the external domain of the unit circle. Coefficients a_n, $n = 1, \ldots, N$, are calculated by an iterative process and the number N depends on the geometrical complexity of the section contour. Normal ship sections require 6–10 coefficients for an accurate representation, while for complex contours (such as at a bulbous bow or stern) 50–60 coefficients may be necessary.

In transformation (1) it is assumed that two symmetry planes exist, i.e. the water plane and the longitudinal ship symmetry plane. If the section contour does not intersect these planes at right

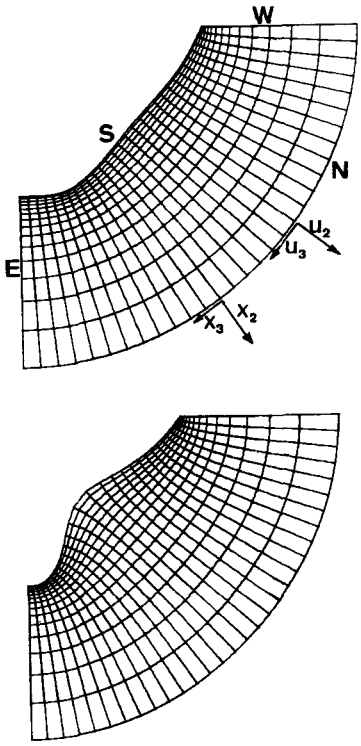

Figure 1. Orthogonal curvilinear grids on transverse sections

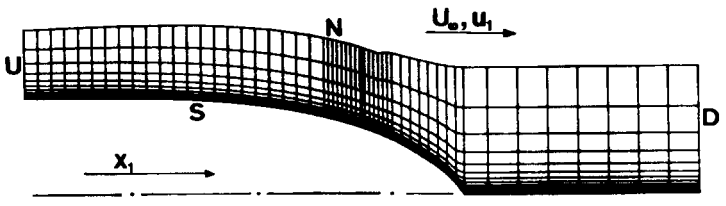

Figure 2. Grid on water plane

angles, a Karman–Trefftz mapping[21] is firstly applied to transform the contour and then (1) is used.

Once the coefficients of the transformation have been calculated for each ship section, orthogonal curvilinear grids on transverse planes can be obtained from the corresponding grids on the circle plane. The latter are formed as intersections of radii and concentric circles, which are defined according to the desired grid arrangement along the section contour and a normal to it. If, in addition to those originally given as data, some intermediate sections are needed to obtain finer resolution in the longitudinal direction, they can be easily produced by cubic interpolation among the transformation coefficients of the adjacent original sections.

Govering transport equations

In a 3D orthogonal curvilinear system (x_i, x_j, x_l) with metrices (h_i, h_j, h_l), where indices i, j, l are in cyclic permutation, the u_i time-averaged momentum (Reynolds) equation reads[14,22]

$$C(u_i)=-\frac{1}{h_i}\frac{\partial P}{\partial x_i}+\rho u_j^2 K_{ji}+\rho u_l^2 K_{li}-\rho u_i u_j K_{ij}-\rho u_i u_l K_{il}+(\sigma_{ii}-\sigma_{jj})K_{ji}+(\sigma_{ii}-\sigma_{ll})K_{li}$$
$$+\sigma_{ij}(2K_{ij}+K_{lj})+\sigma_{il}(2K_{il}+K_{jl})+\frac{1}{h_i}\frac{\partial \sigma_{ii}}{\partial x_i}+\frac{1}{h_j}\frac{\partial \sigma_{ij}}{\partial x_j}+\frac{1}{h_l}\frac{\partial \sigma_{il}}{\partial x_l}, \tag{2}$$

where $C(u_i)$ shows the convection terms, i.e.

$$C(u_i)=\frac{\rho}{h_i h_j h_l}\left(\frac{\partial(h_j h_l u_i^2)}{\partial x_i}+\frac{\partial(h_i h_l u_i u_j)}{\partial x_j}+\frac{\partial(h_j h_i u_i u_l)}{\partial x_l}\right). \tag{3}$$

The stress sensor components on the right-hand side of (2) include both the viscous and the Reynolds stresses and are defined as[23]

$$\sigma_{ii}=2\mu_e e_{ii}=2\mu_e\left(\frac{1}{h_i}\frac{\partial u_i}{\partial x_i}+\frac{u_j}{h_i h_j}\frac{\partial h_i}{\partial x_j}+\frac{u_l}{h_i h_l}\frac{\partial h_i}{\partial x_l}\right),$$
$$\sigma_{ij}=\mu_e e_{ij}=\mu_e\left[\frac{h_j}{h_i}\frac{\partial}{\partial x_i}\left(\frac{u_j}{h_j}\right)+\frac{h_i}{h_j}\frac{\partial}{\partial x_j}\left(\frac{u_i}{h_i}\right)\right], \tag{4}$$

and the curvature terms K_{ij} are expressed as

$$K_{ij}=\frac{1}{h_i h_j}\frac{\partial h_i}{\partial x_j}, \quad i\neq j. \tag{5}$$

If the co-ordinate lines (x_1, x_2, x_3) of the adopted ship co-ordinate system correspond to (x_i, x_j, x_l), the following simplifications are valid:

$$h_1 = 1, \qquad K_{12} = K_{21} = K_{13} = K_{31} = 0, \tag{6}$$

since in each local orthogonal system the x_1-direction is normal to the section plane.

The effective viscosity μ_e in expressions (4) is calculated according to the assumptions of the k–ε turbulence model[16] as follows:

$$\mu_e = \mu + \mu_t = \mu + 0{\cdot}09\,\rho k^2/\varepsilon, \tag{7}$$

where μ_t is the isotropic eddy viscosity, μ is the fluid viscosity, ρ is the fluid density, k is the turbulence kinetic energy and ε is its dissipation rate. The values of k and ε are determined by solving two more differential equations, which in any orthogonal curvilinear system can be written in the form

$$\operatorname{div}\left(\rho\Phi\mathbf{c} - \frac{\mu_t}{\sigma_\Phi}\operatorname{grad}\Phi\right) = S_\Phi, \tag{8}$$

where

$$\Phi = k \text{ or } \varepsilon, \qquad \sigma_k = 1, \qquad \sigma_\varepsilon = 1{\cdot}3,$$

$$S_k = G - \rho\varepsilon, \qquad S_\varepsilon = 1{\cdot}44\,G\frac{\varepsilon}{k} - 1{\cdot}92\,\rho\frac{\varepsilon^2}{k},$$

$\mathbf{c}$ is the mean velocity vector and the generation term G is expressed as

$$G = 2\mu_t[e_{ii}^2 + e_{jj}^2 + e_{ll}^2 + \tfrac{1}{2}(e_{ij}^2 + e_{jl}^2 + e_{li}^2)]. \tag{9}$$

It is usual in computational fluid mechanics to simplify the complete transport equations (2) and (8) whenever a velocity component is dominant along one direction of the flow field. If in the present case this direction is assumed to coincide with the co-ordinate axis x_1 (i.e. parallel to the ship symmetry axis), then the following approximations are often made.

(a) $\partial^2\Phi/\partial^2 x_1 = 0$ for every variable Φ.
(b) Terms including $\partial u_3/\partial x_1$ and $\partial u_2/\partial x_1$ are neglected in expressions of σ_{31} and σ_{21}.
(c) Terms including σ_{31} and σ_{21} are neglected in the u_2- and u_3-momentum equations.

The above simplifications, which have been widely used so far in the well known partially parabolic approach,[24,25] lead to the derivation of the higher-order parabolized-in-x_1 Reynolds equations. Since the corresponding numerical solution requires significantly less computer cost than the solution of the complete equations (being of elliptic type), results obtained by both methods are compared with experiments in the last section of this work.

Discretized equations

Following the finite volume approach,[26] the general transport equations (2) and (8) can be integrated in a control volume surrounding the node P (Figure 3) to obtain an algebriac equation of the form

$$A_P\Phi_P = A_N\Phi_N + A_S\Phi_S + A_E\Phi_E + A_W\Phi_W + A_D\Phi_D + A_U\Phi_U + S_\Phi, \tag{10}$$

where the subscripts N (north), S (south), E (east), W (west), D (downstream) and U (upstream) refer to the neighbouring grid nodes of the central node P. The control volume of each variable is defined according to the staggered grid analysis.[14]

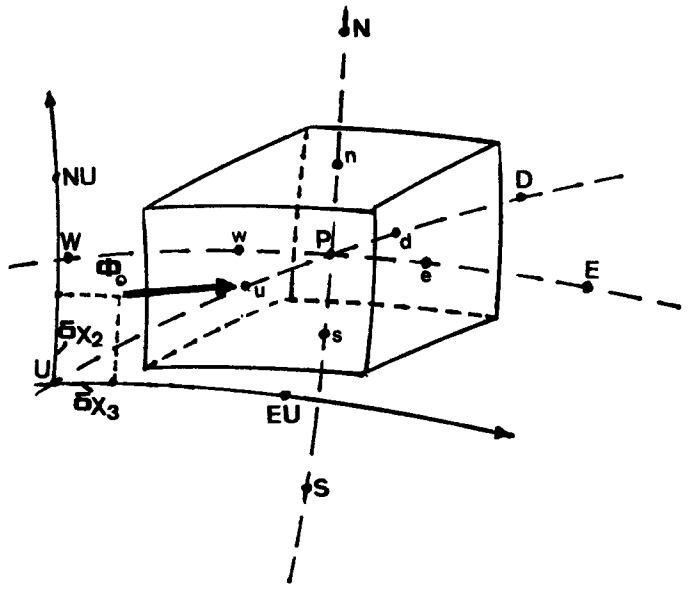

Figure 3. Control volume

The coefficients A_i, $i = \mathrm{N, S, E, W, D, U}$, on the right-hand side of equation (10) are functions of the variable Φ and represent the combined effect of the convection and diffusion terms on the corresponding faces of the control volume. The integrated sum of these terms along the co-ordinate line j which intersects the i-face of the control volume is approximated as[12,14]

$$[C(\Phi)-D(\Phi)]_i^j = C_i\Phi_i - \Gamma_i E_i\left(\frac{\delta\Phi}{\delta x}\right)_i^j, \tag{11}$$

where C_i is the total flux through the i-face, Φ_i is the value of the variable defined on the intersection of the co-ordinate line and the face, Γ_i is the local diffusivity rate at the same location and E_i is the projection of the face area normal to the j-co-ordinate line.

The numerical approximation of coefficients A_i has been the subject of extensive research work, because they are directly related to numerical diffusion errors. The crucial point in all the developed methods is the approximation of the convection term in (11), since the application of higher-order schemes leads in many cases to ill-conditioned coefficient matrices or is unable to satisfy boundedness requirements[12] (this does not hold for diffusion terms which, usually approximated by central differencing, have a favourable contribution). Convergent and bounded solutions are obtained if the following strict condition holds:

$$|A_P| \geqslant \sum_i |A_i|. \tag{12}$$

A lower-order approximation for the modelling of convection and diffusion terms which satisfies (12) is the hybrid scheme proposed by Spalding.[27] This scheme uses central or upwind differencing according to the local Peclet numbers, so that all coefficients A_i in equation (10) are non-negative. Although it leads to unconditionally convergent solutions, its application is advantageous with respect to accuracy whenever the mean velocity vector is aligned to the grid lines.

Obviously, it is difficult to fulfil this requirement in practical problems when complex geometries are examined.

In order to test the effectiveness of the hybrid scheme in the present study, two more exact approximations are also examined. These are the skew upstream scheme[28,29] and the classical central differencing scheme[14] used to model the convection terms in the longitudinal and transverse directions respectively. In any case, to retain conservativity between adjacent systems, the u_2- and u_3-velocity components on the upstream and downstream planes are transformed to the local co-ordinate system of central node P.

Skew upwind differencing is based on the concept that convective transport occurs along streamlines and the value Φ_u of any variable on the upstream face of the control volume shown in Figure 3 equals Φ_o, where $\overrightarrow{ou}$ coincides with the local velocity vector. According to the first-order Taylor expansion, Φ_o is approximated as

$$\Phi_o \approx \Phi_U + \frac{\partial \Phi}{\partial x_2}\delta x_2 + \frac{\partial \Phi}{\partial x_3}\delta x_3. \tag{13}$$

The partial derivatives in (13) are computed using the values of Φ at the main nodes of the upstream system, depending on the location of 'o'. For example, in the case of Figure 3 it is

$$\frac{\partial \Phi}{\partial x_3} \approx \frac{\Phi_{EU} - \Phi_U}{\delta x_{EU-U}}, \qquad \frac{\partial \Phi}{\partial x_2} \approx \frac{\Phi_{NU} - \Phi_U}{\delta x_{NU-U}}. \tag{14}$$

Application of (13) and (14) leads to expressions in 3D analysis equivalent to the 2D case.[14] If the same analysis is followed for the downstream face 'd', the combined effect of upstream and downstream convective terms becomes

$$[\mathrm{Conv}]_u^d = C_u\Phi_U - C_d\Phi_P + \left[C_u\left(\frac{\partial \Phi}{\partial x_2}\delta x_2 + \frac{\partial \Phi}{\partial x_3}\delta x_3\right)_U - C_d\left(\frac{\partial \Phi}{\partial x_2}\delta x_2 + \frac{\partial \Phi}{\partial x_3}\delta x_3\right)_P \right], \tag{15}$$

where C_u and C_d are the fluxes through the upstream and downstream faces of the control volume respectively. If the terms in brackets are included in the sum of source terms of equation (10), the conservative expressions (11) for A_U and A_D are written as

$$A_U = C_U + \frac{\Gamma_U E_U}{\delta x_{PU}}, \qquad A_D = \frac{\Gamma_D E_D}{\delta x_{PD}}. \tag{16}$$

Evidently, these expressions are derived under the assumption that no recirculation in the x_1-direction exists, which is true for the flow around a conventional ship's stern. If in some regions the u_1-component takes negative values, the hybrid scheme is used to compute A_U and A_D. Although the computational cost increases remarkably, one should expect that with the introduction of the skew-upwind system numerical diffusion in x_1 will be reduced, since the co-ordinate systems vary along the ship axis.

The central as well as the skew upstream differencing does not *a priori* satisfy condition (12) and boundedness requirements. However, it was found that, with the proper grid discretization in the longitudinal direction, they can be successfully applied without any convergence problems. This behaviour has been attributed to the high positive values of the u_1-velocity component which characterize the flow field under consideration.

Boundary conditions

Boundary conditions for every variable Φ have to be specified on each boundary of the calculation domain. At the inlet plane U (Figure 2), which is located almost amidships, the values

of the flow variables are calculated using experimental data. For the velocity components u_1 and u_3 it is assumed that the $1/n$ power law is valid, i.e.

$$\frac{u_1}{u_e}=\left(\frac{x_2}{\delta}\right)^{2/(H_{12}-1)}\cos[\Theta(x_2)], \qquad \frac{u_3}{u_e}=\left(\frac{x_2}{\delta}\right)^{2/(H_{12}-1)}\sin[\Theta(x_2)], \tag{17}$$

where u_e is the velocity at the edge of the boundary layer, δ is the local boundary layer thickness, H_{12} is the shape factor and Θ is the cross-flow angle ($\Theta=0$ at $x_2=\delta$). The values of δ, H_{12} and Θ on grid points are calculated by linear interpolation among the corresponding experimental data. If the distribution of the experimental wall shear stress τ_w is also available at points around the inlet section, the velocity distribution in the near-wall region is calculated by the logarithmic law approximation, i.e.

$$\frac{u_1}{u_\tau}=\frac{1}{\kappa}\ln(Ey^+\cos\Theta_b), \qquad \frac{u_3}{u_\tau}=\frac{1}{\kappa}\ln(Ey^+\sin\Theta_b), \tag{18}$$

where $u_\tau=\sqrt{(\tau_w/\rho)}$, $\kappa=0{\cdot}42$, $E=9{\cdot}79$, $y^+=u_\tau x_2/\nu$ and Θ_b is the cross-flow angle at the point of intersection of the profiles defined by (17) and (18). The u_2-component, being almost normal to the body surface, is computed using the linear relation $u_2=x_2u_{2n}/\delta$, where u_{2n} is defined at $x_2=\delta$. The values of u_e and u_{2n} as well as the velocity components on grid nodes out of the boundary layer are calculated from the potential flow solution around the actual body.[30] The distributions of k and ε at the inlet plane are estimated after the experimental data of Klebanoff[31] and Bradshaw *et al.*[32] respectively, scaled according to δ and u_e.[13]

At the external boundary N the velocity components and the pressure are calculated by the potential flow solution and the normal derivatives of k and ε are taken equal to zero. Normal derivatives on the two symmetry planes (i.e. the water plane and the ship symmetry plane) are also equal to zero for variables u_1, u_2, p, k and ε, while for component u_3 the Dirichlet condition $u_3=0$ is valid.

At the outlet plane D of the calculation domain the flow is assumed to be fully developed. The values of the flow variables on this plane are set equal to those of the previous section of the domain, except for the pressure which is linearly extrapolated.

Two methods are followed in this work in order to model the near-wall behaviour, resulting in application of different types of boundary conditions on the solid boundary S. The first of them is the wall function approach[16] based on the assumption that the distribution of the velocity component parallel to the boundary follows the logarithmic law (17) for values of y^+ ranging roughly between 40 and 100. Assuming also that the production of k is almost equal to its dissipation rate, a complete set of boundary conditions for u_1, u_3, k and ε can be obtained and implicitly introduced in equation (10).[14,16] Owing to the staggered non-orthogonal grid which is employed, there is not a simple way to apply the wall function approximation for the calculation of both the coefficient A_s and the value of u_2 on the south face (through P in Figure 4) of the adjacent-to-the-wall control volume when the u_2-momentum equation is solved. If the relative analysis is made according to the assumption that the velocity near the wall is parallel to it, the aforementioned values can be easily obtained using the logarithmic distribution. However, this assumption is not true, since the flow is strongly divergent in the thick boundary layer region of the stern and its application leads to unrealistic overestimation of the velocity profiles. Trying to overcome this problem, a parabolic fitting for u_2 has been adopted, using its values at $x_2=0$ ($u_2=0$) and at the adjacent-to-the-wall nodes. Comparative results with the two approximations are shown in Figure 5, where the calculated longitudinal (U/U_e) and transverse (W/U_e) velocity

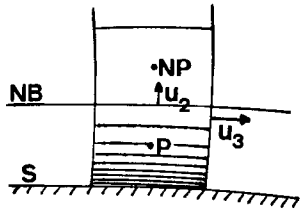

Figure 4. Near-wall treatment

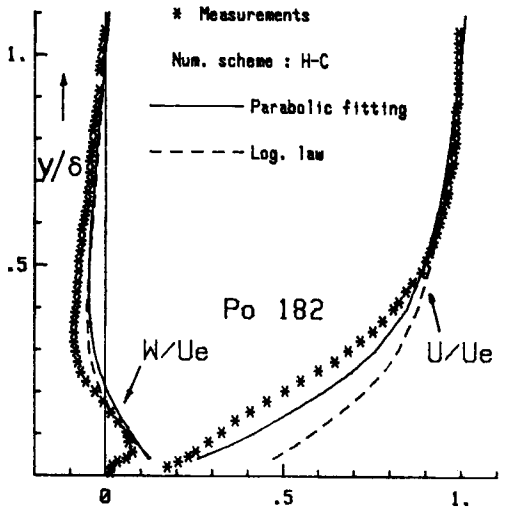

Figure 5. Effect of u_2 treatment (HSVA)

profiles (as explained in the next section) are compared with measurements at a stern point of the HSVA model. It is evident that significantly better results are obtained using the parabolic fitting.

To avoid the shortcomings of the wall function approach, the second method which has been examined is to solve the Reynolds equations up to the solid boundary. The solution is performed by subdividing the original adjacent-to-the-wall cells into a certain number of subcells as shown in Figure 4. The complete u_1- and u_3-momentum equations (2) are solved in these subcells (i.e. below NB) according to the general discretization form (10) and using boundary conditions $u_1 = u_3 = 0$ on the wall. Following the fundamental concept of the parabolic shear layer (PSL) method of Iakovides and Launder,[33] the third velocity component u_2 is calculated explicitly from the integrated form of the continuity equation from the wall ($u_2 = 0$) to the boundary NB. Since the pressure gradients in the x_2-direction are insignificant, simplified relations can be applied to determine the pressure in the subcell region. In the present investigation the pressure values between boundaries S and NB are assumed to vary linearly according to their values at points NP and P. The pressure at NP is calculated by the solution procedure described in the sequel, while its value at P is calculated inversely from the integrated form of the u_2-momentum equation in the control volume which is defined by nodes P and NP. The adoption of this methodology (concerning the calculation of both the u_2-component and the near-wall pressure values) is beneficial to achieve convergence as well as to obtain higher convergence rates than solving the

three momentum and the continuity equations up to the boundary. The latter presents many difficulties owing to the large aspect ratio values of the subcells, which have an unfavourable influence on the velocity–pressure coupling during the iterative solution procedure followed.

The application of k–ε model variants which include modifications for the near-wall turbulence structure has so far proved unsuccesful[34] to calculate adequately the flow quantities, even in simple 2D flows. This has been mainly attributed to the lack of physical information concerning the ε-equation. This is why it was decided to use simplified empirical expressions for the determination of the eddy viscosity μ_t in the inner (i.e. subcell) region. The latter is calculated after the mixing length[35] approximation, i.e.

$$\mu_t = \rho L^2 (\partial u_s / \partial x_n), \tag{19}$$

where x_n is the normal distance from the body surface, u_s is the velocity component normal to x_n and L and denotes the mixing length given by

$$L = \kappa x_n [1 - \exp(-x_n / A_L)], \tag{20}$$

with the Van Driest damping factor A_L calculated as

$$A_L = 26\nu(\tau_w/\rho)^{1/2}.$$

The wall shear stress τ_w equals $\mu(\partial u_s/\partial x_n)$ at $x_n = 0$. The subcells are formed so that at least two grid nodes along x_2 lie within the linear sublayer region, the latter defined by $y^+ < 3$. The k-equation (8) is also solved up to the solid boundary with boundary condition $k = 0$ on the wall. To take into account the near-wall effects, the quantity $-2\nu(\partial k/\partial x_2)^2$ is added to the source term of k according to the low-Reynolds-number model of Launder and Sharma.[34] The calculation of k in the inner region is necessary to obtain boundary conditions for the solution in the outer region. The corresponding values of ε are calculated inversely from (7), i.e. $\varepsilon = 0{\cdot}09\rho k^2/\mu_t$, so that compatibility in the two different expressions (7) and (19) is satisfied at the common boundary NB. Once the k-equation has been solved, the values of eddy viscosity μ_t in the inner region can alternatively be calculated by the one-equation k–L turbulence model[35] as

$$\mu_t = 0{\cdot}09\rho\sqrt{(kL)}. \tag{21}$$

Comparisons between calculated results when expression (19) or (21) is used to define μ_t are also presented in the next section.

For values of y^+ higher than 100 the mixing length expression (19) becomes essentially equal to κx_n. According to simple boundary layer experiments, the adopted value for κ is about 0·4. However, when this predetermined value was used, discontinuity problems appeared at the matching boundary NB of the inner and outer regions, mainly in the calculation of turbulence characteristics. This behaviour is shown in Figure 6, where the u_1-velocity profile and the distribution of the effective viscosity μ_e are plotted with respect to the distance from the solid boundary at a stern point of the SSPA model. The dashed line corresponds to calculated results with $\kappa = 0{\cdot}4$. Evidently, the velocity profile is smooth but the effective viscosity distribution is discontinuous at the matching boundary, where the function κx_n predicts higher values of μ_t than those obtained by the k–ε model in the outer region. This problem is eliminated if the factor κ is calculated so that expressions (7) and (19) (or (21)) give the same value for μ_t at NP, i.e.

$$\kappa = \left[\frac{1}{x_n}\sqrt{\left(\frac{0{\cdot}09k^2/\varepsilon}{(\partial u_s/\partial x_n)}\right)}\right]_{NP}. \tag{22}$$

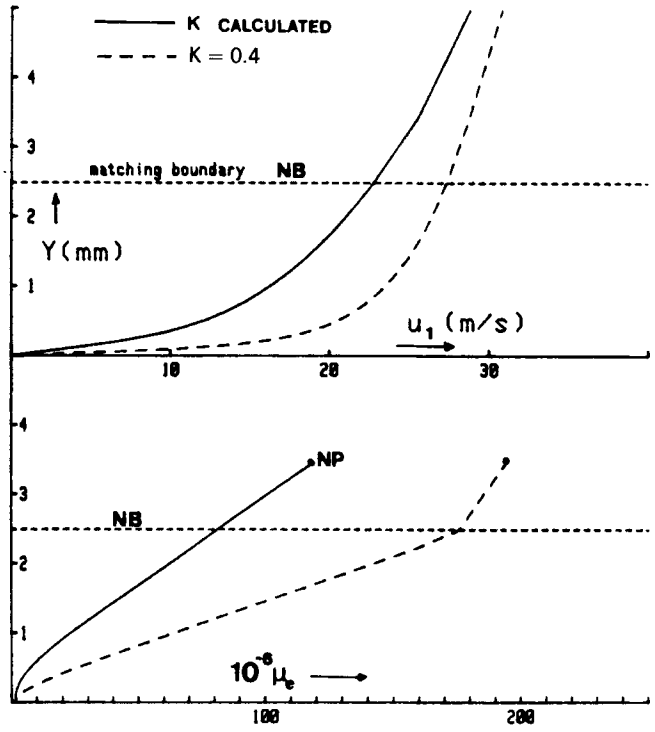

Figure 6. Near-wall velocity and effective viscosity distribution

The above relation implies that κ is a function depending on the local flow parameters and being constant only along a certain normal on the body surface. The results presented by the full line in Figure 6 show how the velocity and effective viscosity values are modified when κ is calculated using (22).

Solution procedure

The dominant flow direction along the x_1-axis, which governs the field under consideration, allows the application of the partially parabolic approach[36] to solve the discretized transport equations (10). An initial guess for the pressure field, based on extrapolation of potential flow values at the external boundary, is made and then a marching solution is performed following successive transverse sections in the calculation domain. At a certain section the momentum equations are firstly solved and in the sequel the velocity components and the pressure are corrected to satisfy continuity according to the SIMPLE algorithm.[14,37] Then the turbulence model equations are solved and the effective viscosities are updated. Calculation steps as above are repeated and, after convergence of local variables has been reached, the solution proceeds in the next sections until a sweep of the domain is completed. Experience has shown that a number of sweeps almost equal to the number of transverse sections is required to obtain overall convergence. Since the velocity field converges faster than the pressure field, the following relation is used as the convergence criterion:

$$\mathrm{RES}(P)<\alpha, \qquad \mathrm{RES}(P)=\frac{\sum^{M}|\Delta P|^{N}}{\sum^{M}|\Delta P|^{1}}, \tag{23}$$

where M is the total number of grid points, ΔP is the pressure change at each grid point after the Nth sweep is completed and α is a constant. For the Reynolds numbers tested it has been found that when $\alpha = 0{\cdot}02$, the maximum change of u_1-component between two successive sweeps is below 0·1%. A typical curve showing the convergence rate of the normalized pressure residuals as a function of the number of sweeps is given in Figure 7. The corresponding calculations have been carried out for the HSVA model using 55 transverse sections with a 30×30 transverse node density.

When the Reynolds equations are solved up to the solid boundary (as described previously), an internal iterative solution is furthermore required in order to obtain convergence within the subcell region. Then the calculated boundary values are used to solve the equations in the outer region in a single step and the same procedure is repeated until local convergence is achieved. This decoupling is advantageous since, to reduce the required computer cost, a relatively fast solution with the wall function method is firstly obtained and then the direct wall simulation is applied using the original grid. Moreover, different solid boundaries (appendages) can be treated independently.

Convergence of each transport equation is obtained using underrelaxation according to the following transformation of the original equation (10):

$$A'_p = A_p/r, \qquad A'_p \Phi_n = \sum A_i \Phi_{in} + S_\Phi + (1-r) A'_p \Phi_0,$$

where r is the underrelaxation factor, Φ_o is the old value of the variable Φ and Φ_n is the updated one.[38]

TEST CASES

As already mentioned in the Introduction, the SSPA[17] and HSVA[19] models have been used as test cases to evaluate the numerical calculations. Both of them were tested experimentally in wind tunnels but the measurements of the stern velocity profiles were taken using different techniques (hot wire for the SSPA and pitot tubes for the HSVA model). The body plans together with the locations of the aftermost measuring points on the body surface are shown in Figures 8(a) and 8(b). Velocity measurements were taken along normals to the model surface directions starting from these points (11–15 for the SSPA and 180–185 for the HSVA model). The experimental

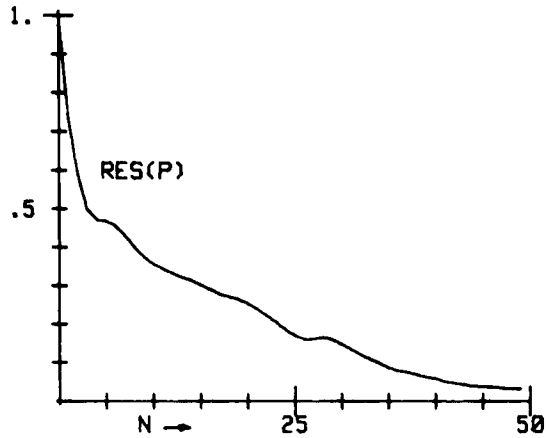

Figure 7. Normalized pressure residual versus number of sweeps, N

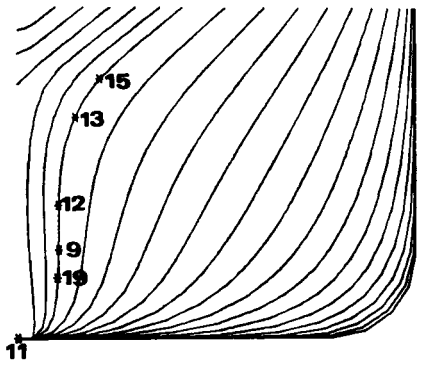

Figure 8(a). Body plan of SSPA model

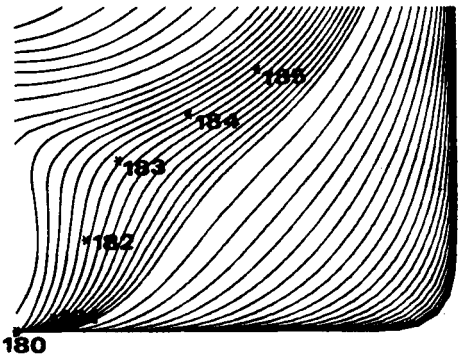

Figure 8(b). Body plan of HSVA model

results concerning the above measurements are presented as longitudinal (U/U_e) and transverse (W/U_e) velocity profiles versus the non-dimensionalized normal distance y/δ, where δ is the local boundary layer thickness. Longitudinal profiles are calculated as projections of the velocity vectors on the plane which is defined by the normal on the surface and the velocity U_e at the edge of the boundary layer. Transverse velocity profiles are obtained as corresponding projections on the normal-to-U_e plane and are positive towards the keel of the ship. Results for the skin friction coefficient $C_F=\tau_w/\frac{1}{2}\rho U_\infty^2$ and the pressure coefficient $C_p=(P-P_\infty)/\frac{1}{2}\rho U_\infty^2$ are also presented at the same locations as functions of the contour length (girth). Experiments were carried out at a Reynolds number equal to 5×10^6 for the SSPA and $6{\cdot}8\times10^6$ for the HSVA model.

The test cases for which calculations were performed are shown in Table I. These differ according to the numerical scheme employed, the grid density and the near-wall treatment (wall functions or direct solution). The first letter in the notation H–C, S–C, etc. denotes the numerical scheme used to model the convection terms along the x_1-direction, i.e. hybrid (H) or skew upwind (S). The second letter shows the scheme used in the transverse directions, i.e. hybrid (H) or central (C). In the notation $NI\times NJ\times NK$ used to specify the grid density, NI is the number of grid nodes around the girth of a section (x_3-direction), NJ is the number of nodes along the normal (x_2-direction) and NK is the number of transverse sections. The inlet planes of the calculation domains were placed at $x/L=0{\cdot}55$ and $x/L=0{\cdot}6$ for the SSPA and HSVA models respectively (L is the model length and x is the longitudinal distance from the bow). At these sections experimental data necessary to calculate the input conditions are available. The corresponding exit planes were placed at $x/L=1{\cdot}2$ and $x/L=1{\cdot}4$. In both cases the distance of the external boundary was at least three times the maximum measured boundary layer thickness, while the values of y^+ in the adjacent-to-the-wall grid nodes ranged between 30 and 150. The input, exit and external boundaries were the same in every test. A special interpolation output programme was developed to calculate the velocity profiles at the experimental points, since the computed flow variables are stored in different locations. All computations were carried out on a SUN-330 SPARC station.

Evaluation of numerical schemes

Comparisons of the calculated velocity profiles, skin friction and pressure coefficients using various combinations of numerical schemes, i.e. central (C), hybrid (H) or skew upwind (S), are shown for the two models in Figures 9–13. The computations were carried out with a $32\times30\times45$

Table I. Test cases

	Numerical scheme	Grid size $NI \times NJ \times NK$
SSPA	H–H (w.f.)	32 × 30 × 45 (w.f., direct)
	H–C	45 × 30 × 45 (w.f., direct)
	S–H	32 × 30 × 63 (w.f.)
HSVA	H–H (w.f.)	15 × 15 × 53 (w.f.)
	H–C	32 × 30 × 53 (w.f., direct)
	S–C	45 × 30 × 53 (w.f., direct)

Wall treatment: w.f., wall functions; direct, up to the wall.

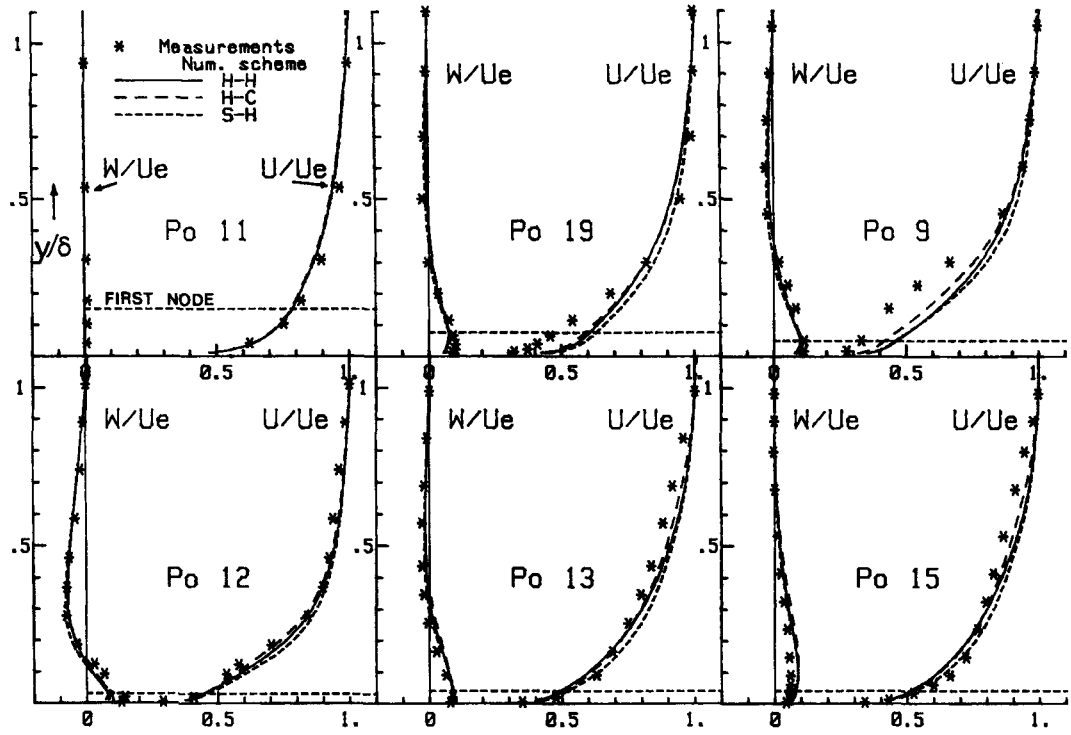

Figure 9. Comparison of velocity profiles for SSPA model

grid for the SSPA model and a 32 × 30 × 53 grid for the HSVA model. The wall function method has been adopted in any case.

In Figure 9 the longitudinal and crosswise velocity profiles are compared with experimental values at points 11–15 of the SSPA model. Three numerical schemes are tested, i.e. H–H (solid lines), H–C and S–H (dashed lines). As observed, the three schemes show similar trends. The calculated longitudinal velocity profiles are in very good agreement with the measured values at points 11–13 and 15, while all computations overestimate the longitudinal velocity component in the near-wall region around points 19 and 9. These points are located in the region where the

most rapid changes of the stern geometry occur. It should be noticed here that the dashed horizontal line shows the position of the first near-wall node and the profiles below this line are extrapolated according to the logarithmic wall law. The H–C scheme seems to have the better behaviour with respect to the measurements, implying that the adoption of a higher-order scheme in the transverse directions is more important than improving the upstream convective terms. The agreement between the calculated and experimental crosswise velocity profiles is very good at all points, whether the corresponding components change sign in the normal direction (e.g. point 12) or not. This is crucial for the prediction of the longitudinal vortex formation which influences the resistance and propulsion characteristics of a ship. Corresponding comparisons for the HSVA model are shown in Figure 10, where the H–H, H–C and S–C schemes are tested. The calculated longitudinal and crosswise profiles at points 180 and 181, lying in the keel region, are in very good agreement with the measured values. Differences are again observed at point 182, where the computed longitudinal profiles have higher values than the experimental ones, while at point 183 the velocity components are underpredicted with respect to experiments for $y/\delta < 0{\cdot}2$. In this region the measured longitudinal profile presents an inflection point associated with high positive values of crosswise components. Similar behaviour but with less intense differences is observed at point 184, while calculations are in good agreement with experiments at point 185 which is located near the water plane. The H–C scheme again produces the best results, whereas with the adoption of central differences the S–C combination is relatively improved. However, the differences among the calculated profiles are still of minor importance.

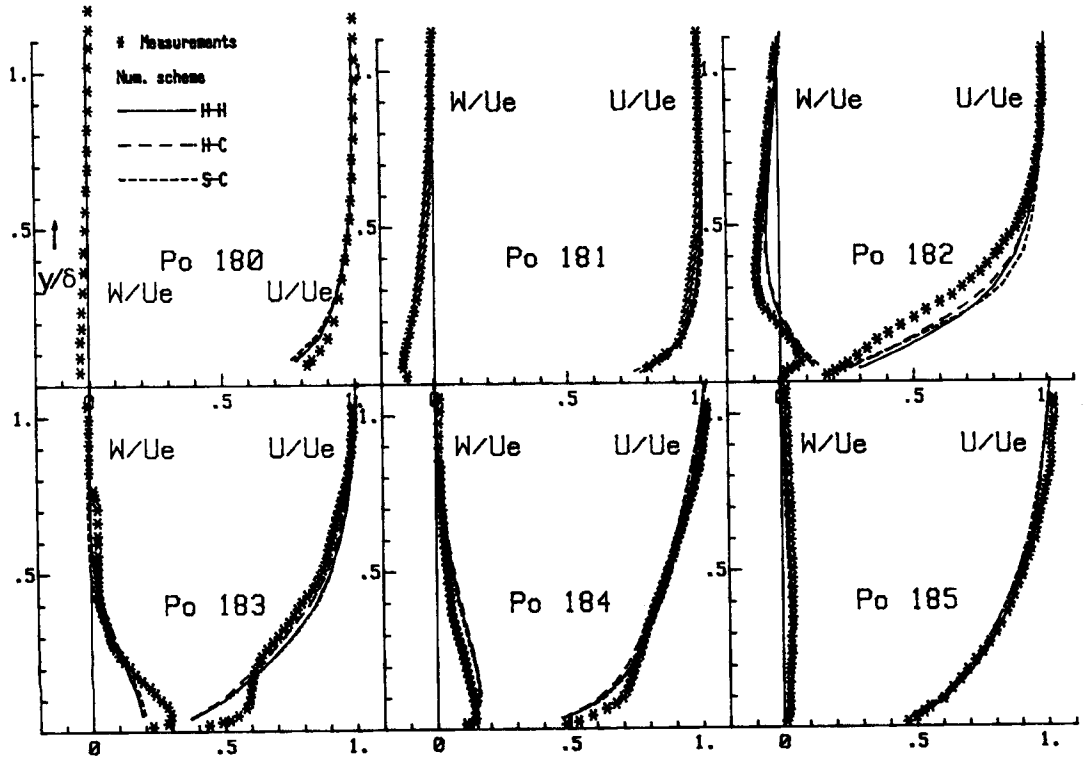

Figure 10. Comparison of velocity profiles for HSVA model

Comparisons of the skin friction coefficient C_F for the SSPA model are shown in Figure 11. The numerical schemes tested give practically the same results, which are in satisfactory agreement with the experimental data, the latter being deduced from the measured velocity profiles. This is not the case for the HSVA stern section, where the rapid variation of the stern geometry causes steep changes of the flow parameters girthwise as shown in the experimental results of Figure 12. The experimental C_F-values have been either directly measured (Preston tubes) or implicitly derived from the velocity profiles (Clauser or Ludwieg–Tillman method). The calculated results, slightly improved by the application of the S–C scheme, tend to underestimate the skin friction values in the region of points 183 and 184, i.e. where a velocity defect is observed in the calculated longitudinal profiles (Figure 10). In contrast, the predicted pressure coefficient C_p is in good agreement with the measurements as shown in Figure 13. Also, it is evident from Figure 13 that the potential flow solution fails to predict adequately the pressure field around the stern (related C_p-comparisons are not given here for the SSPA model because the experimental results are influenced by blockage effects). The large opposite-sign pressure gradients existing around the minimum of the C_p-curve near the keel imply a concentration of the flow lines in this region, which is combined with a maximum in the C_F-curve (Figure 12).

The comparisons made in Figures 9–13 indicate that the application of the skew upwind scheme in the x_1-direction has not yielded noticeably or systematically better results than the hybrid scheme. This behaviour implies that the changes in the longitudinal direction of transverse derivatives of any variable Φ are less important than the changes in Φ itself, owing to the dominance of the u_1-component combined with the adopted smoothly varying body-fitted grid.

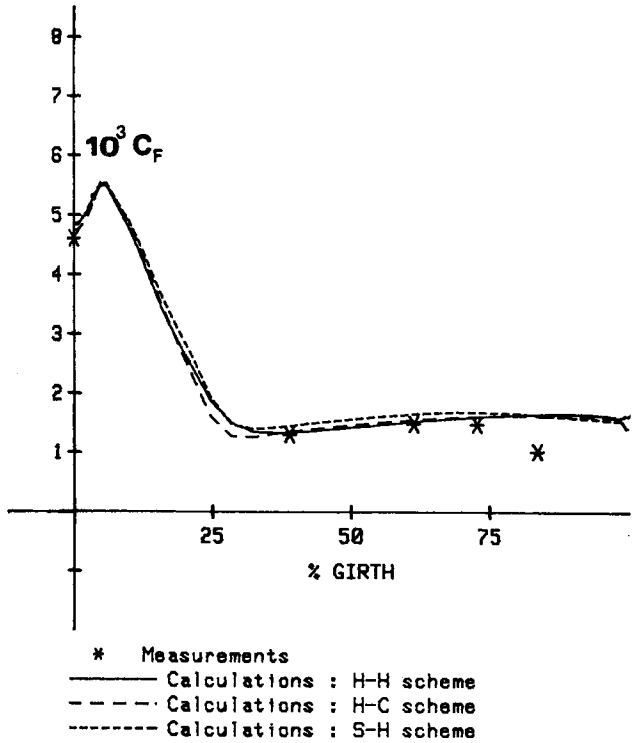

Figure 11. Comparison of C_F-values (SSPA)

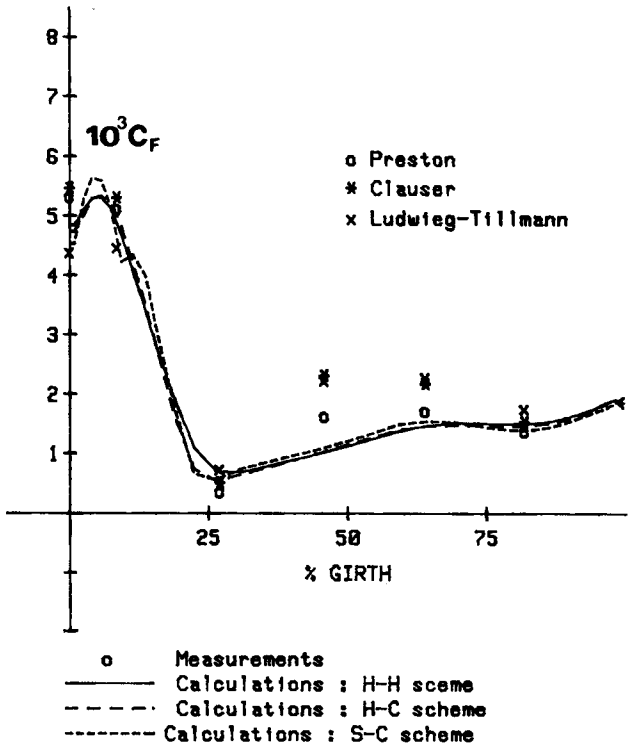

Figure 12. Comparison of C_F-values (HSVA)

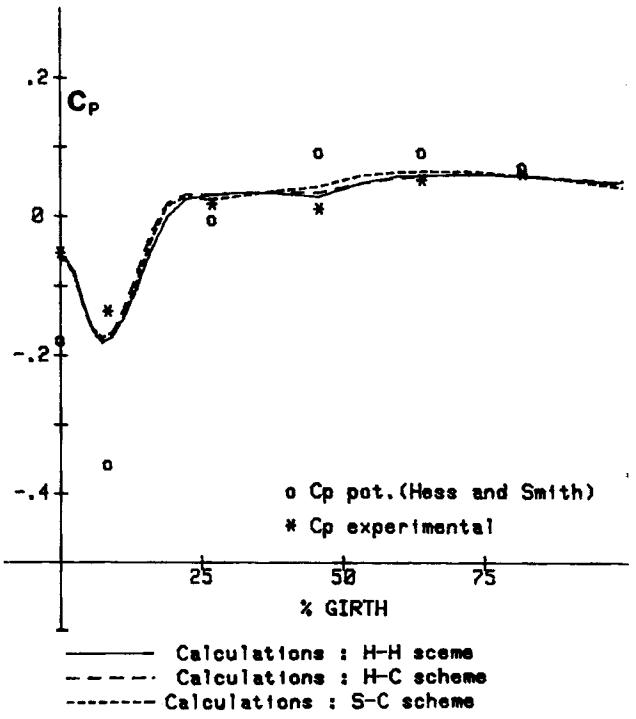

Figure 13. Comparison of C_p-values (HSVA)

Thus the term in brackets in relation (15) is of minor importance compared with the convective terms of the classical upstream scheme, resulting essentially in the same values for coefficients A_U and A_D.

Grid dependence tests

Using the H–C scheme and the wall function method, comparative calculations with various grid sizes have been performed for the two models. The effect of the longitudinal grid refinement, i.e. the number of transverse sections used, has been examined for the SSPA model. Two runs were carried out corresponding to a $32 \times 30 \times 45$ and a $32 \times 30 \times 63$ grid. In the second case 18 more transverse sections were interpolated at the stern region. The results for the velocity profiles have shown only slight improvements with the finer grid. The same trends have been observed when two different girthwise grid densities were compared having respectively $45 \times 30 \times 45$ and $32 \times 30 \times 45$ nodes. The improvement with the finer grid in this case, occurring near the wall at points 13 and 15, was found to be negligible.

The effect of the transverse grid refinement on the calculated results has also been examined for the HSVA model. Three grid sizes, i.e. $45 \times 30 \times 53$, $32 \times 30 \times 53$ and $15 \times 15 \times 53$, were tested. Remarkably better results were obtained with the 32×30 grid than with the coarse 15×15 grid. However, the calculated results did not seem to improve significantly with further girthwise grid refinement concentrated in a region surrounding points 182–184. This behaviour is observed in Figure 14, where the calculated C_F-values are compared with measurements.

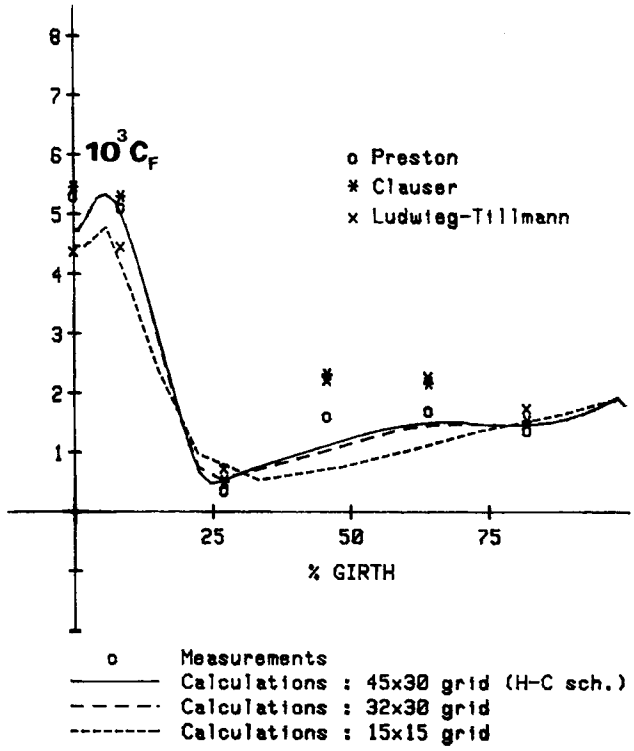

Figure 14. Comparison of C_F-values (HSVA)

Calculations with parabolized equations

Calculations performed using the parabolized-in-x_1 transport equations are compared with those obtained by the complete equations in Figures 15–17. The H–C scheme has been employed and the grids tested had $32 \times 30 \times 45$ nodes for the SSPA and $32 \times 30 \times 53$ for the HSVA model. It is clear from Figure 15 that the solution of the complete equations gives better results in comparison to the measured velocity profiles of the SSPA model. The differences between the two solutions are more pronounced in Figure 16 for the HSVA model, especially around the upper half of the section (i.e. at points 183–185). In this case there is a systematic trend of the parabolized solution to predict lower values of the velocity, which is also implied in Figure 17 where the skin friction is plotted.

Numerical experiments have indicated that the differences between the two methods are due partly to the original assumptions made to derive the parabolized equations and partly to their numerical treatment (the numerical analysis has been based on the strict parabolic form, i.e. the downstream values of different values are assumed to be equal to those calculated at the running section). The application of a certain numerical scheme also seems to affect the related comparisons, since previous comparisons[15] have shown that using the H–H scheme, the above differences are decreased.

Effect of near-wall treatment

In order to compare the results obtained with the wall function method, additional computations were carried out for both models solving the Reynolds equations up to the solid

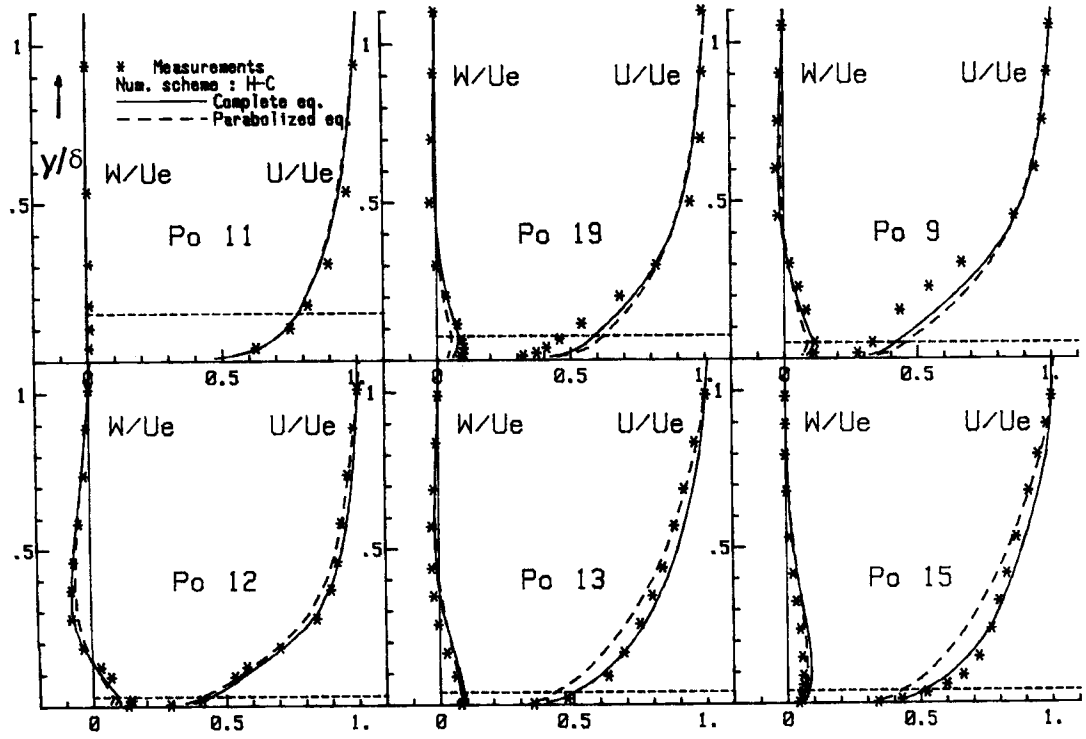

Figure 15. Comparison of velocity profiles for SSPA model

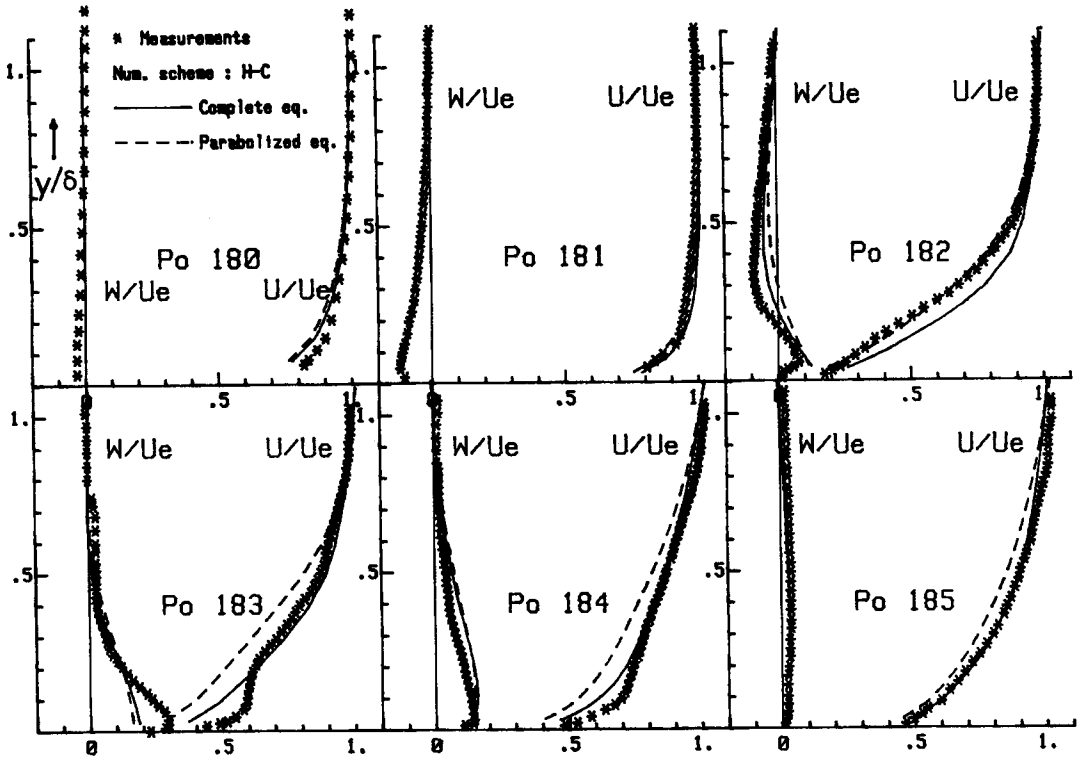

Figure 16. Comparison of velocity profiles for HSVA model

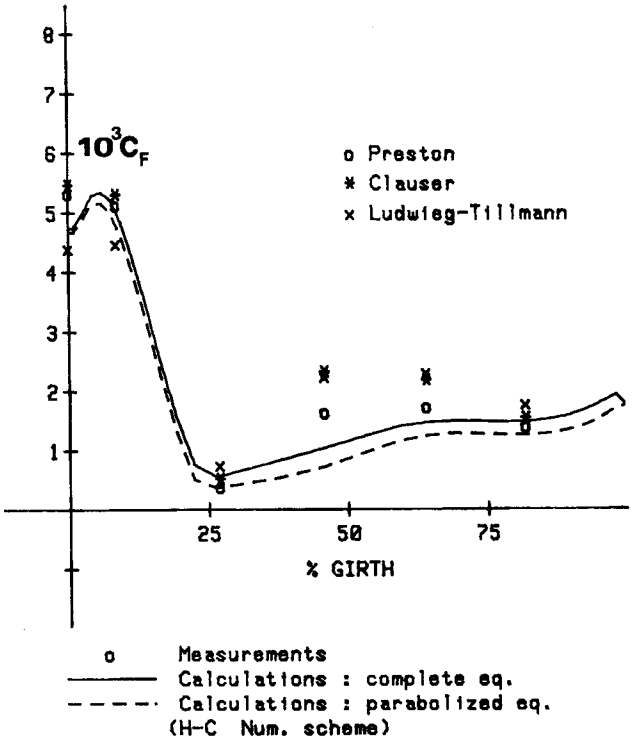

Figure 17. Comparison of C_F-values (HSVA)

boundary, as previously described. The original adjacent to-the-wall cells were subdivided into 20 subcells, resulting in effective transverse grid sizes of 32×50 nodes. In all calculations the H–C scheme was used.

Calculated velocity profiles using the direct near-wall treatment for the SSPA model are compared with experimental values in Figure 18. Calculations correspond to three different approximations of the eddy viscosity in the near-wall region, i.e. the zero-equation (or mixing length) model (19) with an implicitly calculated κ-factor (equation (22)), the one-equation model (21) where κ is again calculated and the zero-equation model using a constant value for κ equal to 0·4. It is clear that in the first two cases significantly better results have been obtained at points 19 and 9. Moreover, no substantial differences are observed between the calculations made with the zero- or one-equation model with adjustable κ-factor. With all approximations tested there is still a tendency to overestimate the longitudinal velocity profile near the solid boundary around point 9. The same trends are shown in Figure 19, where comparative tests are made for the HSVA model. It is obvious that the use of variable κ-values leads to systematically better predictions, but the differences between calculations and measurements at points 182–184 remain. Further girthwise grid refinement results in unimportant improvements, as has been observed by comparing the 32×50 grid with a finer grid having 45×50 nodes.

Calculated values of the skin friction coefficient obtained by the up-to-the-wall solution are compared with measurements of the HSVA model in Figure 20. Computations were carried out using the zero-equation model with adjustable κ-factor. The solid line shown in this figure corresponds to C_F calculated on the solid boundary, i.e. within the linear sublayer. The dashed

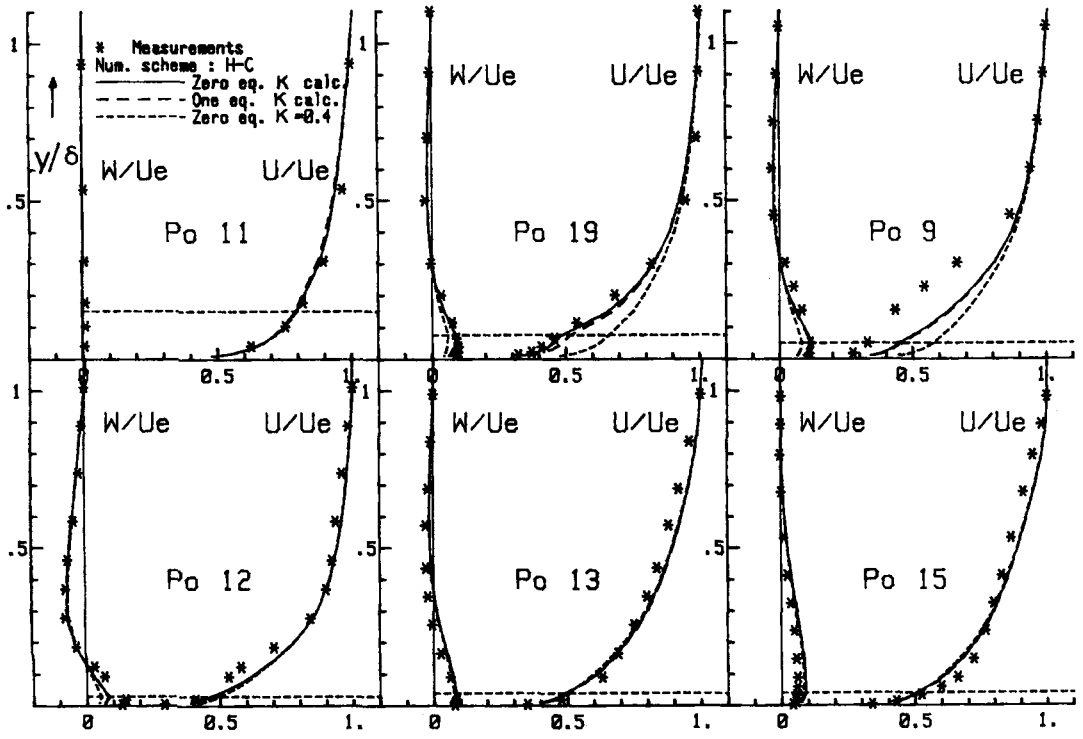

Figure 18. Effect of near-wall treatment on velocity profiles (SSPA)

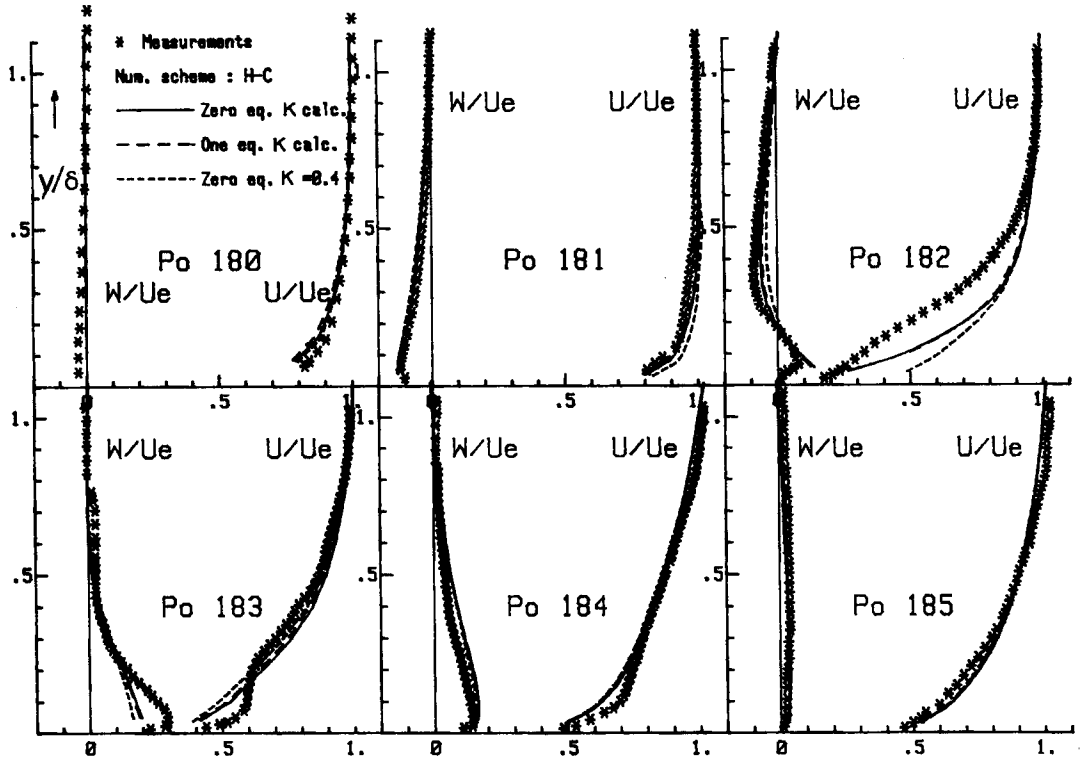

Figure 19. Effect of near-wall treatment on velocity profiles (HSVA)

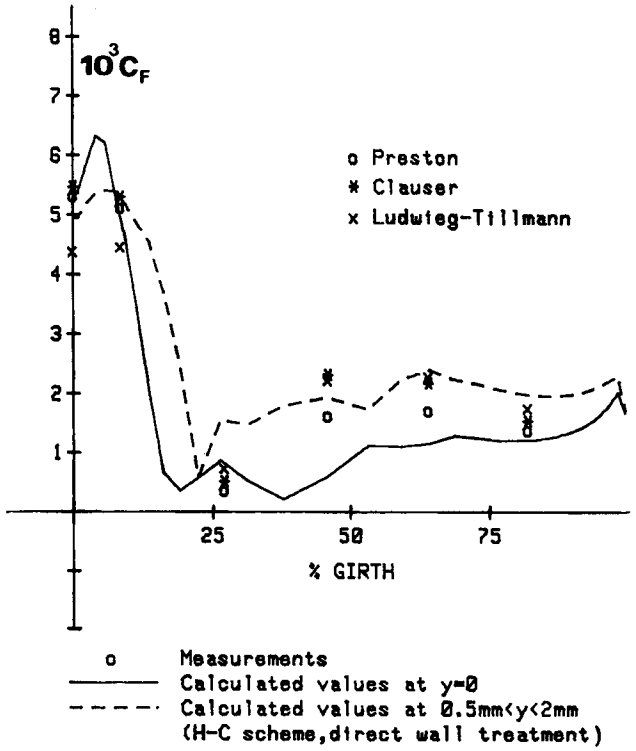

Figure 20. Comparison of C_F-values (HSVA)

line shows the C_F-values derived from shear stress calculations at the centres of the original boundary cells, where the wall function approximations are assumed to hold. Two remarkable conclusions can be drawn. Firstly, there is a substantial difference between the values of the two curves, indicating that the shear stress along the normal to the wall is varying. The wall function approach is based on the assumption that this stress is constant. Secondly, the direct C_F measurements, made by Preston tubes of 1 mm diameter, are located (with a small deviation near point 182, i.e. at 26% of girth) within the range defined by the two curves. This is also valid in general for the experimental C_F derived from the velocity profiles. It must be noticed here that even the direct measurements of C_F suffer from experimental uncertainties, since the size of a Preston tube influences the flow field around it. The same trends have been observed for the stern section of the SSPA model.

Finally, in Figure 21 comparative results of C_p are plotted around the HSVA section using the three near-wall turbulence models. Excellent agreement between calculations and experimental values is observed in the two cases which calculate κ-factors. Also, comparing Figures 13 and 21, the above predictions are better than those obtained with wall functions. In contrast, when κ is assumed to be constant, the calculated C_p-curve is not in close agreement with the measurements.

The numerical tests described in this section, concerning either the application of different numerical schemes and grid resolutions or different near-wall treatments, imply that the differences observed between the calculated and measured velocity profiles are due to the shortcomings of the turbulence model employed. These differences are of two kinds according to the trends of the numerical solutions presented in Figures 9–21. The first kind of difference is associated with

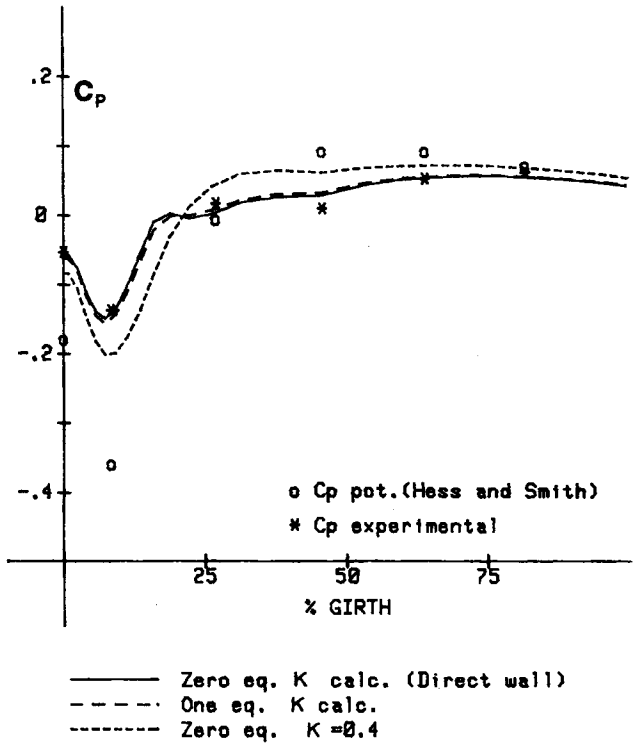

Figure 21. Comparison of C_p-values (HSVA)

the overprediction of the longitudinal velocity components near the solid boundary at stern points where the longitudinal curvature is large, such as points 9 and 19 of the SSPA or point 182 of the HSVA model. Quite similar trends for the SSPA model have been recently presented by Chen *et al.*[39] using a different numerical method based on the finite analytic approximation. This is a well known behaviour of the k–ε model, occurring even in the case of simple axisymmetric stern flows.[40] Comparisons between calculated and experimental Reynolds stresses[14,39] show that the model tends to overestimate the Reynolds stresses near the body surface, resulting in an increase of the velocity components. The second kind of difference is observed near point 183 of the HSVA model, where the experimental longitudinal velocity profile shows an inflection point. Unfortunately, there are no turbulence measurements to be compared with calculated values, but it is expected that the smooth variation of the turbulence characteristics predicted by the k–ε model cannot produce velocity profiles of the above type.

Despite the aforementioned problems associated with the turbulence model, it must be kept in mind that the main interest in ship hydrodynamics is the flow calculation at high Reynolds numbers ($\sim 10^9$). Existing experiments[41] indicate that the longitudinal velocity profiles at these Reynolds numbers become typical boundary-layer-type profiles, which has also been verified by numerical tests.[11] Moreover, the propeller action has an accelerating effect in the stern region where the lower values of the longitudinal components are measured.[42] Consequently, the application of the k–ε turbulence model may be more effective when the real problem is faced. Unfortunately, the latter can be established only by comparisons with experiments at full scale, which are difficult to carry out.

CONCLUDING REMARKS

Various numerical tests have been performed using different finite volume approximations and near-wall models to calculate the stern flow past two double-ship hulls. According to the presented comparisons with existing experimental data, the following conslusions can be drawn.

1. The application of central differencing on transverse-to-the ship axis directions leads to better predictions than the hybrid scheme. In contrast, the use of skew upwind differencing in the longitudinal direction produces almost the same results as the hybrid scheme.
2. The calculated results when the complete equations are solved are in some cases in substantially better agreement with the measurements than those obtained by the parabolized equations.
3. The direct solution of the Reynolds equations in the near-wall region is almost insensitive to the turbulence models which have been employed (i.e. the simple mixing length or the one-equation k–L model). The corresponding results are drastically affected by the treatment of the proportion factor κ of the mixing length formula. If the latter is implicitly calculated to match with the outer solution, remarkable improvement in the calculated values is obtained.
4. The comparisons of the calculated velocity profiles using either the wall function method or the direct solution of the Reynolds equations up to the wall show similar trends. However, quite different results are obtained for the skin friction coefficient C_F.
5. The application of the k–ε turbulence model seems to be responsible for some discrepancies observed between calculated and experimental velocity profiles, especially at the stern region where rapid changes in the geometry occur. However, further numerical as well as experimental work is needed to validate the model in the case of a high-Reynolds-number flow past a ship.

REFERENCES

1. *Proc. 18th Int. Towing Tank Conf.*, The Society of Naval Architects of Japan, Kobe, 1987.
2. J. P. Comstock (ed.), *Principles of Naval Architecture*, SNAME, New York, 1967, pp. 293–300.
3. L. A. Larsson, L. H. Broberg, P. H. Zhang and K. J. Kim, 'New viscous and inviscid CFD techniques for ship flows', *Fifth Int. Conf. on Numerical Ship Hydrodynamics*, Hiroshima, 1989.
4. G. K. Politis and K. Belibasakis, 'Application of panel methods in linearized lifting surface propeller performance problem', *Fifth IMAEM Congr.*, Hellenic Institute of Marine Technology, Athens, 1990, pp. 373–380.
5. V. C. Patel, 'Ship stern and wake flows: status of experiments and theory', *17th ONR Symposium on Naval Hydrodynamics*, The Hague, 1988, pp. 1–20.
6. L. Larsson (ed.), *1990 SSPA–CTH–IIHR Workshop on Ship Viscous Flow*, SSPA, Göteborg, 1990.
7. A. K. Rastogi and W. Rodi, 'Calculation of general 3D turbulent boundary layers', *AIAA J.*, **16**, 151–159 (1978).
8. H. C. Chen and V. C. Patel, 'Practical near-wall turbulence models for complex flows including separation', *AIAA Paper 87-1300*, Honolulu, 1987.
9. J. Piquet and M. Visoneau, 'Computation of the flow past ship-like hulls', *Fifth Int. Conf. on Numerical Ship Hydrodynamics*, Hiroshima, 1989, pp. 278–295.
10. M. Hoekstra, 'Recent developments in a ship stern flow prediction code', *Fifth Int. Conf. on Numerical Ship Hydrodynamics*, Hiroshima, 1989, pp. 55–69.
11. G. D. Tzabiras and T. A. Loukakis, 'On the numerical solution of the turbulent flow-field past double ship hulls at low and high Reynolds numbers', *Fifth Int. Conf. on Numerical Ship Hydrodynamics*, Hiroshima, 1989, pp. 395–408.
12. A. D. Gosman and K. Y. M. Lai, 'Finite difference approximations for the transport and Navier–Stokes equations', *IAHR Symp. on Refined Modelling of Flows, Report FS/82/18*, Imperial College of Science and Technology, Paris, 1982, pp. 1–35.
13. G. Tzabiras and T. Loukakis, 'A method for predicting the flow around the stern of double ship hulls', *Int. Shipbuilding Prog.* **345**, 94–105 (1983).
14. G. Tzabiras, 'Numerical and experimental investigation of the flow field at the stern of double ship hulls', *Ph.D. Thesis*, National Technical University of Athens, 1984.
15. G. Tzabiras, 'On the calculation of the 3-D Reynolds stress tensor by two algorithms', *Second Int. Symp. on Ship Viscous Resistance*, SSPA, Göteborg, 1985, pp. 15.1–15.16.
16. B. E. Launder and D. B. Spalding, 'The numerical computation of turbulent flows', *Comput. Methods Appl. Mech. Eng.*, **3**, 269–289 (1974).
17. L. Larsson, 'Boundary layers of ships', *Ph.D. Thesis*, Chalmers University, Göteborg, 1975.
18. L. Lofdahl, 'Measurements of the Reynolds stress tensor in the thick 3D boundary layer near the stern of a ship model', *Ph.D. Thesis*, Chalmers University, Göteborg, 1982.
19. H. P. Hoffmann, 'Untersuchung der 3-dimensionalen, turbulenten Grenzschicht an einem Schiffsdoppel-modell im Windkanal', *Inst. P. Schiffbau, Bericht 343*, Hamburg, 1975.
20. C. von Kerczek and E. O. Tuck, 'The representation of ship hulls by conformal mapping techniques', *J. Ship Res.*, **19**, 284–298 (1969).
21. C. von Kerczek and F. stern, 'The representation of ship hulls by conformal mapping functions: fractional maps', *J. Ship Res.*, **27**, 158–159 (1983).
22. S. B. Pope, 'The calculation of turbulent recirculating flows in general orthogonal coordinates', *J. Comput. Phys.*, **26**, 197–217 (1978).
23. G. K. Batchelor, *An Introduction to fluid dynamics*, Cambridge University Press, Cambridge, 1979.
24. A. M. Abdelmeguid, N. C. G. Markatos and D. B. Spalding, 'A method of predicting three-dimensional turbulent flows around ships hulls', *First Int. Symp. on Ship Viscous Resistance*, SSPA, Göteborg, 1978, pp. 3.1–3.24.
25. A. M. Abdelmeguid, N. C. Markatos, D. B. Spalding and K. Muraoka, 'A comparison between the parabolic and partially-parabolic solution procedures for 3D turbulent flows around ships' hulls, *J. Appl. Math. Modelling*, **3**, 249–255 (1980).
26. P. J. Roache, *Computational Fluid Dynamics*, Hermosa, Albuquerque, NM, 1972.
27. D. B. Spalding, 'A novel finite difference formulation for differential expressions involving both first and second derivatives', *Int. j. numer. methods eng.*, **4**, 551–559 (1972).
28. G. D. Raithby, 'Skew upstream differencing schemes for problems involving fluid flow', *Comput. Methods Appl. Mech. Eng.*, **9**, 153–164 (1974).
29. M. A. Leschziner, 'On the problem of numerical diffusion in first-order finite-difference schemes applied to free recirculating flows', *Proc. 2nd GAMM Conf. on Numerical Methods in Fluid Mechanics*, Cologne, 1977, pp. 104–112.
30. J. L. Hess and A. M. O. Smith, 'Calculation of potential flow about arbitrary bodies', *Prog. Aeronaut. Sci.*, **8**, 1–138 (1966).
31. P. S. Klebanoff, 'Characteristics of turbulence in a boundary layer with zero pressure gradient', *NACA Rep. 1247*, 1953, pp. 1–19.
32. P. Bradshaw, D. Ferris and N. P. Atwell, 'Calculation of boundary layer development using the turbulent energy equation', *J. Fluid Mech.*, **28**, 593–616 (1967).
33. H. Iakovides and B. E. Launder, 'PSL—an economical approach to the numerical analysis of the near-wall, elliptic flow', *ASME J. Fluids Eng.*, **106**, 241–242 (1984).

34. V. C. Patel, W. Rodi and G. Scheuerer, 'Turbulence models for near wall and low Reynolds number flows: a review', *AIAA J.*, **23**, 1308–1319 (1985).
35. B. E. Launder and D. B. Spalding, *Mathematical Models of Turbulence*, Academic, London/New York, 1972.
36. V. S. Pratap and D. B. Spalding, 'Numerical computations of the flow in curved ducts', *J. Aeronaut. Sc.*, **26**, 219–232 (1975).
37. S. V. Patankar and D. B. Spalding, 'A calculation procedure for heat, mass and momentum transfer in 3-D parabolic flows', *Int. J. Heat Mass Transfer*, **15**, 1787–1806 (1972).
38. J. P. Doormal and G. D. Raithby, 'Enhancements of the SIMPLE method for predicting incompressible fluid flows', *Numer. Heat Transfer*, **7**, 147–163 (1984).
39. H. C. Chen, V. C. Patel and S. Ju, 'Solutions of Reynolds-averaged Navier-Stokes equations for 3D incompressible flows', *J. Comput. Phys.*, **88**, 305–336 (1990).
40. G. D. Tzabiras, 'A numerical investigation of the turbulent flow-field at the stern of a body of revolution', *J. Appl. Math. Modelling*, **11**, 45–61 (1987).
41. K. Taniguchi and T. Fujita, 'Comparison of velocity distribution in the boundary layer between ship and model', *Selected papers from Journal of Society of Naval Architects of Japan*, **9**, 79–87 (1972).
42. K. Yokoo, H. Takahashi, M. Narato, Y. Yamazaki, H. Tanaka and T. Ueda, 'Comparison of wake distributions between ship and model', *Selected papers from Journal of Society of Naval Architects of Japan*, **11**, 25–36 (1973).